Published in final edited form as:
*J Magn Reson*. 2012 January ; 214(1): 212–220. doi:10.1016/j.jmr.2011.11.010.

# Evaluation of non-selective refocusing pulses for 7 T MRI

**Jay Moore**[a,b,1,*], **Marcin Jankiewicz**[a,b,1], **Adam W. Anderson**[a,b,c], and **John C. Gore**[a,b,c]

Jay Moore: jay.moore@vanderbilt.edu; Marcin Jankiewicz: m.jankiewicz@vanderbilt.edu

[a]Vanderbilt University Institute of Imaging Science, 1161 21st Ave. South, MCN AA-1105, Nashville, TN 37232-2310

[b]Department of Radiology and Radiological Sciences, Vanderbilt University, 116 21st Ave. South, MCN CCC-1106, Nashville, TN 37232-2675

[c]Department of Biomedical Engineering, Vanderbilt University, 5824 Stevenson Center, VU Station B 351631, Nashville, TN 37232

## Abstract

There is a continuing need for improved RF pulses that achieve proper refocusing in the context of ultra-high field (≥ 7 T) human MRI. Simple block or sinc pulses are highly susceptible to RF field inhomogeneities, and adiabatic pulses are generally considered too SAR intensive for practical use at 7 T. The performance of the array of pulses falling between these extremes, however, has not been systematically evaluated. The aim of this work was to compare the performances of 21 non-selective refocusing pulses spanning a range of durations and SAR levels. The evaluation was based upon simulations and both phantom and *in vivo* human brain experiments conducted at 7 T. Tested refocusing designs included block, composite block, BIR-4, hyperbolic secant, and numerically optimized composite waveforms. These pulses were divided into three SAR classes and two duration categories, and, based on signal gain in a 3-D spin echo sequence, practical recommendations on usage are made within each category. All evaluated pulses were found to produce greater volume-averaged signals relative to a 180° block pulse. Although signal gains often come with the price of increased SAR or duration, some pulses were found to result in significant signal enhancement while also adhering to practical constraints. This work demonstrates the signal gains and losses realizable with single-channel refocusing pulse designs and should assist in the selection of suitable refocusing pulses for practical 3-D spin-echo imaging at 7 T. It further establishes a reference against which future pulses and multi-channel designs can be compared.

### Keywords

refocusing; composite radio frequency pulses; RF field inhomogeneity; 7T; high-field human brain imaging; BIR-4; hyperbolic secant; phase modulation; frequency modulation



[*]Corresponding author. Address: Institute of Imaging Science, Vanderbilt University, 1161 21st Ave. South, MCN AA-1105, Nashville, TN 37232-2310.

[1]Authors contributed equally to this work.

## 1. Introduction

Imaging protocols reliant upon the non-selective refocusing of transverse magnetization (e.g., 3-D versions of spin-echo (SE), turbo spin-echo (TSE), and gradient spin-echo (GraSE) [1] sequences) typically employ either block- or sinc-shaped refocusing pulses resulting in flip angles that scale with the integral of the transmitted RF ( $B_1^+$) field intensity. Adiabatic pulses (e.g., BIR [2, 3] and the hyperbolic secant [4, 5, 6]) as well as composite pulses (e.g., the 3-part pulse of Levitt and Freeman [7] and the version-S pulse of Poon and Henkelman [8, 9]) provide refocusing options with varying degrees of insensitivity to $B_1^+$ and $B_0$ field variations. Although these and other related pulses [10, 11, 12, 13, 14, 15, 16, 17, 18] have been considered for use in ultra-high field (≥ 7 T) human brain imaging, the relative performance and SAR limitations of such pulses remain largely enigmatic in this context. In response to the need for a systematic comparison of refocusing pulses for this application, the present study was undertaken with the goals of (1) identifying pulse designs that could potentially improve refocusing performance at 7 T within practical limits of SAR, (2) modifying or redesigning such pulses to achieve performance that is specifically focused on 7 T brain imaging, (3) simulating the refocusing characteristics of chosen pulses given actual measurements of static ($B_0$) and $B_1^+$ field distributions at 7 T, and (4) measuring the signal gains obtainable with the selected pulses. The results of this work will assist in the selection of suitable refocusing pulses for given applications as well as form a basis for establishing the performance limits of practical refocusing pulses executed on a single transmission channel.

To ensure a degree of practicality, we limited the scope of our studies to refocusing pulses of limited duration and SAR. Pulse designs considered in this study include: a 180° block pulse; a 3-part composite of block pulses [7]; a rendition of the version-S pulse [8]; a set of BIR-4 pulses [3]; a set of hyperbolic secant (HS) pulses [19, 20]; and a set of optimized composite pulses (OPT-C) [21, 22]. The BIR-4, HS, and OPT-C pulses were all numerically optimized to enhance refocusing performance over a targeted range of $B_1^+$ and $\Delta B_0$ values representative of those encountered in the human brain at 7 T [23]. Three different SAR constraints and two different total durations were enforced during these optimizations, thus resulting in six BIR-4, six HS, and six OPT-C pulses. In total, 21 waveforms were evaluated. Theoretical pulse performances were investigated via simulation of magnetization responses over ranges of relevant $B_0$ and $B_1^+$ values. The actual measured signal gains resulting from each pulse are reported relative to the signal obtained using a 180° block pulse in the context of a 3-D SE sequence with a single-shot, echo-planar imaging (EPI) readout. Experiments were performed in both a 17 cm spherical phantom and the *in vivo* human brain at 7 T.

## 2. Theory

Following an excitation pulse of arbitrary phase, an RF pulse with a 180° flip angle and arbitrary phase will result in complete refocusing of transverse magnetization lost to $T_2'$ decay. Underlying this statement are the assumptions that the refocusing pulse is executed at a time $T_E/2$ halfway between the excitation and signal acquisition and that $B_1^+$ field inhomogeneity does not alter the effective flip angle of the pulse. When variations in the $B_1^+$ field are present, a refocusing pulse with a nominal flip angle ($\beta_0$) of 180° will result in in an actual rotation angle given by $\beta_0 \cdot B_1^+ / B_{1,\mathrm{nom}}^+$ where $B_{1,\mathrm{nom}}^+$ is the nominal, unaffected RF field strength. In these terms, on-resonance signal intensity for a SE sequence with repetition time $T_R$ can be expressed as

$$S_{\mathrm{SE}}=M_0 B_1^- \left|\sin\left(\frac{\alpha_0 B_1^+}{B_{1,\mathrm{nom}}^+}\right)\right| \sin^2\left(\frac{\beta_0 B_1^+}{2B_{1,\mathrm{nom}}^+}\right)\times\left(1-e^{-T_R/T_1}\right)e^{-T_E/T_2^*}, \quad (1)$$

where $M_0$ is the equilibrium magnetization, $B_1^-$ is the relative intensity of the RF field associated with reception, $\alpha_0$ is the nominal flip angle of the RF pulse used for excitation, $T_1$ is the time constant of longitudinal relaxation, and $T_2$ is the time constant of transverse relaxation due to non-reversible mechanisms. This relationship implies that, for a given value of $B_1^+/B_{1,\mathrm{nom}}^+$ and a fixed value of $\alpha_0$, the maximum achievable signal occurs in the event that $\beta_0 \cdot B_1^+/B_{1,\mathrm{nom}}^+=\pi$ radians (i.e., the actual flip angle of the refocusing pulse is 180°).

To assess performance differences among refocusing pulses with respect to $B_1^+$ and $\Delta B_0$ it is most straightforward to calculate a ratio of signal intensities so that dependencies on receive profile and relaxation effects are removed from the images. When calculating such ratios of images from sequences with the same excitation pulse, the same $T_E$, and the same $T_R$ but different refocusing pulses (as is the case in the present study), all factors in Equation 1 are common with the exception of the $\beta$-dependent argument of the $\sin^2$ function. Thus, the ratio of signals $S_{\mathrm{SE};1}$ and $S_{\mathrm{SE};2}$ is expressible as

$$\frac{S_{\mathrm{SE},1}}{S_{\mathrm{SE},2}}=\frac{\sin^2(\beta_{0,1}B_1^+/(2B_{1,\mathrm{nom}}^+))}{\sin^2(\beta_{0,2}B_1^+/(2B_{1,\mathrm{nom}}^+))}. \quad (2)$$

Signal ratios for all pulses evaluated in this study are determined through experiment but reflect the value expressed in Equation 1 with $S_{\mathrm{SE};2}$ representing the signal of the block pulse with $\beta_0$= 180°.

For simulations and numerical optimizations, we adopted a Cartesian magnetization space ($M_x$, $M_y$, $M_z$) in which reversal of the transverse magnetization phase implies a change in direction of one of the transverse magnetization components, i.e., ($M_x$, $M_y$, $M_z$) is changed to either ($M_x$, $-M_y$, $-M_z$) or ($-M_x$, $M_y$, $-M_z$). Such phase reversals can be accomplished through 180° rotations about the *x* or *y* axes, as is the case when employing a 180° block pulse for refocusing. If the notation $M_i^{XYZ}$ is adopted to indicate the *i*-th component of magnetization following an RF pulse given the initial conditions $(M_x^{\mathrm{init}}, M_y^{\mathrm{init}}, M_z^{\mathrm{init}})=(X, Y, Z)$, the action of an effective refocusing pulse can be characterized by one of the following: 1) $M_x^{100}=-1$ and $M_y^{010}=1$ or 2) $M_x^{100}=1$ and $M_y^{010}=-1$. Thus, the refocusing capability of any RF pulse can be evaluated through examination of the quantity $|M_x^{100}+M_y^{010}|$, which is equal to zero in the ideal case. In this study, this same measure is used to determine theoretical refocusing performance and is the subject of minimization for all numerical pulse optimizations (see Section 3.1).

# 3. Methods

## 3.1. Pulse designs

The refocusing pulses chosen for evaluation in this study are described as follows and hereafter referred to with the given nomenclature. All amplitude and phase modulation waveforms are presented in Figure 1.

**BLK—**This is the shortest duration block-shaped pulse that results in an volume-averaged flip-angle of 180°. Because the commercial power optimization of the Philips 7 T scanner results in the nominal flip-angle being attained for only regions with the highest $B_1^+$ (i.e., the center of the imaging volume), it was necessary in practice to adjust the nominal flip angle such that the largest volume-averaged signal was achieved. This equated to a 50% net-flip-angle increase (i.e., the nominal flip angle according to the scanner was 270°). Peak amplitude was set to the maximum allowed value of 15 $\mu$T such that duration was minimized and bandwidth maximized. This choice along with the desired power adjustment resulted in a total duration of 1.05 ms.

**COMP3—**This is the three-part composite rotation ( $90^\circ_x - 180^\circ_y - 90^\circ_x$, with subscripts indicating the axis of rotation) designed by Levitt and Freeman [7]. In our implementation of the pulse, the amplitude of each block-shaped component is set to the maximum RF amplitude of 15 $\mu$T in order to achieve maximum bandwidth. Calibrating power to maximize volume-averaged signal in the same manner as was used for the BLK pulse resulted in a total pulse duration of 2.10 ms.

**VS—**This pulse is the 16-component 5.4$\pi$ composite pulse (version-S) developed by Poon and Henkelman [8] following modification by means of the same 50% power increase used with the previously described pulses. After scaling the RF amplitude of all sub-pulses such that the sub-pulse with the highest flip-angle had an amplitude of 15 $\mu$T, sub-pulse durations were adjusted so as to achieve 150% of the flip-angles prescribed in the original publication. This resulted in sub-pulse durations of 806.4 $\mu$s and a total pulse duration of 12.9 ms.

**BIR-4—**These pulses are based upon four-part, $B_1$-insensitive rotations with 180° nominal flip angles ( $\Delta\varphi_{\mathrm{RF}} = \frac{3}{2}\pi$) defined according to the RF modulation function in the original BIR-4 publication [3]. In order to accommodate the potential for different targeted echo times, we chose to implement these pulses at durations of 6.5 ms and 12.9 ms. Numerical optimization of the six parameters determining the amplitude, phase, and frequency modulation of the BIR-4 waveforms [3] was performed on a relevant grid of $B_1^+$ and $\Delta B_0$ values according to the methods described in Section 3.2. Optimizations were repeated with three different SAR constraints (referred to as *low*, *moderate*, and *high*), thus resulting in a total of six different BIR-4 pulses.

**HS—**These are variants of the hyperbolic secant pulses as described by Silver et al. [19, 20]. The parameters $A_0$, $\mu$, and $\beta$ that are responsible for the shape of the amplitude and frequency/phase modulations were the subject of numerical optimizations in the same manner as with the BIR-4 pulses described above. The same two durations and three SAR levels used in BIR-4 optimizations were also enforced in the HS optimizations, thus resulting in a total of six HS pulses. The non-linear phase of HS pulses is problematic for slice-selective imaging and is often compensated through using composites of such pulses [5, 6]; however, for 3-D imaging with non-selective pulses, the non-linear phase is permissible such that only a single HS pulse is required for refocusing.

**OPT-C—**These numerically optimized composite pulses consist of a series of block-shaped components, each having constant amplitude and constant phase. Optimization is performed as described in Section 3.2 and in the same manner as was adopted for the BIR-4 and HS pulses. OPT-C pulses, however, were comprised of either 101 or 202 sub-pulses, thus affording 202 and 404 free optimization parameters, respectively (i.e., one phase and one amplitude for each sub-pulse). Sub-pulse durations were fixed at 64 $\mu s$ such that total pulse durations were either 6.5 ms (in the case of 101 sub-pulses) and 12.9 ms (in the case of 202 sub-pulses). Amplitudes were allowed to range from 0 to 15$\mu T$, and phase was free to vary over the entire range of $\pm\pi$ radians. As with the BIR-4 and HS pulses, three different SAR constraints were applied during the optimizations, thus resulting in a total of six OPT-C pulses. Similar composite refocusing pulse designs have been previously reported (e.g., [7, 8, 9, 17, 22, 24]); however, the OPT-C pulses introduced in this study are, to our knowledge, the first such pulses to be both SAR-limited and specifically designed for use in the human brain at 7 T.

### 3.2. Numerical optimizations

As described in the previous section, numerical optimizations were used to tune all BIR-4, HS, and OPT-C pulses in this study for use in the brain at 7 T. For the first two of these pulse types, it is the global parameters defining the amplitude, phase, and frequency modulation patterns that are optimized, and, for the latter type, it is the individual phases and amplitudes of the sub-pulses that are subject to optimization. All optimizations were carried out on discrete grids of $B_1^+/B_{1,\mathrm{nom}}^+$ and $\Delta B_0$ values with respective ranges of [0.2 1.0] and ±100 Hz as justified by field values measured in the human brain at 7 T (e.g., Figure 2 and [21]). Although the measured *in vivo* distribution of $\Delta B_0$ typically extends beyond ±100 Hz, the choice to target this range in optimizations is motivated by the expectation that the region of acceptable pulse performance in the $B_1^+ - \Delta B_0$ grid would extend somewhat beyond the designated region of interest. Optimization routines were written in Matlab (The MathWorks, Natick, MA) and employ the fmincon function with the interior-point algorithm (a gradient-descent method) to handle minimization of the cost function

$$\delta = \frac{1}{n\,m}\sum_{i,j=1}^{n,m} W_{ij}\cdot\left|M_{x,ij}^{100}+M_{y,ij}^{010}\right|, \tag{3}$$

where $i$ and $j$ are indices on the $B_1^+ - \Delta B_0$ ($n \times m$ dimensional) optimization grid on which the magnetization responses were simulated, $W$ contains the relative weights of each grid point, and $M_x^{100}$ and $M_y^{010}$ are the transverse components of magnetization as described in Section 2. The latter were found through simulation of the Bloch equation for the refocusing pulse under consideration. In all cases, $(W)_{ij}=(B_1^+/B_{1\,\mathrm{nom}}^+)_{ij}^{-1}$ such that pulse performance at low $B_1^+$ values was favored over that at high values. This choice helps offset the fact that the cost function is more easily satisfied at high $B_1^+$ values.

SAR constraints were incorporated into the optimization of each refocusing pulse by requiring that a minimum possible repetition time ($T_{R;\mathrm{min}}$) dictated by the maximum allowed SAR ($\mathrm{SAR}_{\mathrm{max}}$ = 3 W/kg [25]) be less than a specified limit ($T_{R,\mathrm{lim}}$). The relationship

$$\mathrm{SAR}=\frac{C}{T_R}\int_0^{\Delta T}|A(t)|^2dt, \tag{4}$$

in which $A(t)$ is the amplitude modulation function and $C$ is a coil specific constant describing the rate of energy dissipation of 298 MHz radiation in human brain tissue, can be inverted such that the minimum $T_R$ is given by

$$T_{R,\min}=\frac{C}{\mathrm{SAR}_{\max}}\int_0^{\Delta T}|A(t)|^2dt. \tag{5}$$

SAR constraints were then incorporated into optimizations by requiring $T_{R,\min} \leq T_{R,\lim}$. Optimized pulses were generated in three separate SAR classes by specifying three distinct limiting $T_R$ values: $T_{R,\lim}$ = 200 ms (defining a *low-SAR* class of pulses), $T_{R,\lim}$ = 400 ms (defining a *moderate-SAR* class of pulses), and $T_{R,\lim}$ = 600 ms (defining an *high-SAR* class of pulses). During optimizations, calculation of $T_{R,\min}$ included the SAR contributions of both the given refocusing pulse and a 90° block-shaped excitation pulse with a peak amplitude of 15 $\mu$T; thus, the equivalent values of $T_{R,\lim}$ considering only the refocusing component were 120 ms, 320 ms, and 520 ms for the low-, moderate-, and high-SAR classes, respectively.

### 3.3. Simulation methods

All simulations of magnetization responses to RF pulses in this study were based on a rotation matrix formulation of a relaxation-independent form of the Bloch equation [26]. The OPT-C pulses naturally lend themselves to such calculations. Pulses with continuously varying modulations (i.e., the BIR-4 and HS pulses) were divided into discrete, 6.4 $\mu$s steps over which the phase and amplitude were considered to be constant. This step length represents the dwell time of the digital RF amplifier, and the discretization accurately reflects the way in which continuous waveforms are executed on such hardware. For all pulses, magnetization response to the appropriate composite of $k$ sub-pulses, each with constant phase and amplitude, was modeled as a series of rotations ($R_j$, where $j$ = 1, …, $k$). With each rotation corresponding to one of the $k$ individual sub-pulses, the collective operation of all such components of a pulse is described by

$$\mathbf{M}^{\mathrm{final}}=R_kR_{k-1}R_{k-2}\ldots R_1\mathbf{M}^{\mathrm{init}}. \tag{6}$$

### 3.4. Imaging protocols

All experiments were conducted on a 7 T Philips Achieva whole body scanner (Philips Health-care, Best, the Netherlands) based on a Magnex (Varian Medical Systems, Palo Alto, CA) 90 cm magnet. RF transmission and reception was carried out with a single-channel, quadrature volume head coil from Nova Medical (Wilmington, MA). All phantom experiments used a 17 cm dielectric phantom from FBIRN (Function Biomedical Information Research Network) with relaxation constants of $T_1/T_2^*$=1150/42 ms as measured at 7 T. For *in vivo* experiments, one volunteer (female, 56 y.o.) was recruited from the community, and written informed consent was obtained according to the guidelines of the local Institutional Review Board.

Static field maps were obtained in the phantom and human subject using a 3-D GRE sequence with a double-echo acquisition ($\Delta T_E$ = 1 ms). Scan resolution was 3×3×3 mm within a 240×192×135 field of view in the anterior-posterior, right-left, and foot-head directions, respectively. Maps of $B_1^+/B_{1,\text{nom}}^+$ were calculated via a voxel-by-voxel fitting of signal intensities from a multi-flip-angle, multi-slice, multi-shot GRE-EPI scan ($T_R$ = 5000 ms, EPI factor = 5) [27, 28]. Slices were oriented in the transverse plane with no inter-slice gap, and the resolution and field of view were identical to those of the $B_0$ scan. For a given imaging volume, the same projection-based, second-order volume $B_0$ shim currents and power calibrations were used during collection of all data. In addition to providing a measure of the overall distribution of the static field in the imaging volume, $B_0$ maps were used to perform EPI distortion corrections of the $B_1^+$-mapping data [29].

Imaging experiments for evaluating refocusing pulse performance employed a SE-EPI sequence composed of an excitation pulse, a refocusing pulse, and a planar, single-shot EPI acquisition. This fast-imaging protocol was selected to allow a scan with whole-brain coverage to be conducted in approximately 90 s, making it possible to repeat the scan 21 times with different refocusing pulses. The excitation waveform—a Gaussian-modulated sinc pulse with a nominal flip angle of 90°— was executed in the presence of a weak selection gradient so as to reduce signal from outside the designated imaging volume. Refocusing pulses were executed such that the center of the waveform corresponded to the sequence time $T_E/2$ = 27.5 ms. Echo and repetition times were fixed to $T_E/T_R$ = 55/2000 ms with only the RF waveform of the refocusing pulse being modified between subsequent experiments.

## 4. Results and Discussion

Results with integrated discussion are presented in three parts: (1) a short description of the phantom and human brain static and RF field maps with a discussion of the ways these measurements facilitate interpretation of experimental results; (2) presentation of the simulation data for all considered refocusing pulses with a discussion of the utility and practical limitation of such simulations; (3) presentation of phantom and in vivo experimental results exhibiting the varying degree of improvement in signal intensity observed for the refocusing pulses under consideration.

### 4.1. $B_1^+$ and $B_0$ field measurements

Measurements of the $B_1^+$ and $\Delta B_0$ fields for central axial slices of the FBIRN phantom and the human brain as well as 2-D histograms reflecting the whole-volume field distributions are shown in Figure 2. The latter representation indicates the normalized density of voxels in discrete intervals of $B_1^+$ and $\Delta B_0$. As a means of filtering noise and focusing attention on regions of statistical significance, intervals for which the relative voxel density is < 0.001 (i.e., < 0.001% of the maximum value of 1.0) have been masked. The fact that $B_1^+$ measurements for both the phantom and the brain are so heavily congregated around the respective values of 0.5 and 0.6 emphasizes the relative importance of power calibration. Specifically, a proper power adjustment, as is made in the case of the BLK pulse of this study, can result in excellent refocusing performance for the vast majority of voxels in the brain at 7 T. Increasing signal in the relatively few number of voxels with outlying values of $B_1^+$ is the purpose of the other refocusing pulses investigated in this study. In terms of absolute range, $B_1^+/B_{1\,\text{nom}}^+$ variations are slightly larger in the phantom [~ 0.4, ~ 1.2] than in the brain [~ 0.3, ~ 0.9], but static field variations are much less pronounced in the phantom ($|\Delta B_0| \lesssim 40$ Hz) than in the brain ($|\Delta B_0| \lesssim 150$ Hz). These observations suggest that

refocusing performance limits with regard to $B_1^+$ are pushed further in the case of the phantom experiments while the opposite is true for $\Delta B_0$. It is particularly noteworthy with respect to interpreting signal gain measurements that refocusing performance in the center of the phantom where $B_1^+/B_{1\,\mathrm{nom}}^+ > 1$ may not be relevant to human subjects at 7 T, although attention to such regions may be helpful in predicting potential refocusing performance in the brain at higher field strengths.

### 4.2. Simulations

Simulated values of $|M_x^{100} + M_y^{010}|$, which describe refocusing performance as discussed in Section 2, are presented for a grid of relevant $B_1^+$ and $\Delta B_0$ values in Figure 3. The presentation order corresponds to that of the RF waveforms in Figure 1. For many pulses, refocusing performance by this measure appears remarkably similar, especially within the targeted optimization region (indicated by the white dashed box). This observation—that the performance differences among the evaluated pulse designs are often subtle—is alone an important outcome of the present study. For example, the fact that a 6.5 ms HS pulse with moderate SAR can be designed to achieve similar refocusing at 7 T as a BIR-4 of similar SAR and twice the duration is useful information that, to our knowledge, has not been established. Inspection of the actual cost function values (Equation 3) appearing in Table 1 facilitates many such comparisons. Expectedly, higher SAR pulses are generally capable of better refocusing as are longer pulses of the same SAR class; however, for either a given SAR class or a given duration, the OPT-C pulses always result in the lowest cost function values. This observation is also of relative importance, suggesting that OPT-C pulses provide the most flexible solution to the problem of field-insensitive, non-selective refocusing in the face of demanding limitations on duration and SAR. Figure 3 also emphasizes the bandwidth limitations of the various pulses. At least in regions of relative high $B_1^+$ (e.g., $B_1^+/B_{1,\mathrm{nom}}^+ = 0.8 - 1.0$), the COMP3 pulses appears most robust in the face of large static field variations and therefore represents an attractive pulse choice when effective $B_0$ shimming is most challenging. Furthermore, it is evident that longer pulses are more difficult to design with high bandwidth, thus lending a slight advantage to the shorter (6.5 ms) pulses, although longer pulses clearly have an edge when it comes to $B_1^+$-insensitivity.

Also appearing in Table 1 are the SAR-related values of $\int |A(t)|^2\, dt$ and $T_{R,\mathrm{min}}$ (Equation 5) for each pulse. These numbers reveal that SAR-limited optimizations are largely effective in the creation of three distinct SAR-classes based on the criteria given in Section 3.2. One exception to this is the high-SAR, 6.5 ms HS pulse for which the optimization, due to the given constraints and the nature of the HS modulations, converges to a SAR value intermediate to the moderate and high classes. The only other noteworthy exception is perhaps the BLK pulse for which SAR is significantly greater than for the other pulses assigned to the same class. This latter observation illuminates the fact that a variety of numerically optimized pulses can be designed to outperform an appropriately calibrated block pulse in terms of $B_1^+$-insensitive refocusing while simultaneously allowing for reduced SAR. For example, the low-SAR, 12.9 ms OPT-C pulse offers both an almost two-fold improvement in theoretical refocusing capability (as measured by the cost function value) and a ~ 25% reduction in SAR. Of course, the SAR of the BLK pulse could be significantly reduced at the cost of a lower bandwidth by reducing the peak amplitude and lengthening the duration. This approach might be useful in some SAR-demanding sequences (such as TSE), although, again, no degree of $B_1^+$-insensitivity would be possible.

### 4.3. Experiments

Figure 4 shows 3-D SE-EPI signal intensities (relative to those of the BLK pulse) in the center axial slice of the phantom for all 21 refocusing pulses. Signal gains over the entire 3-D volume are represented in Figure 5 on a grid of $B_1^+ - \Delta B_0$ values. The latter representation is the result of calculating the average signal gain for all voxels within each $B_1^+ - \Delta B_0$ interval on the grid. Using the same noise masking described in Section 4.1, only signal gains corresponding to regions on the grid with relative voxel densities ≥ 0.001% are reported. Focusing on the relatively small $\Delta B_0$ values observed in the phantom, the measured signal gains can be seen to correlate well with the simulation results of Figure 3. For example, improved refocusing performance relative to the BLK pulse is confined to regions of either high or low $B_1^+$, as is expected for all pulses close to resonance. In general, long (12.9 ms) pulses outperform their shorter (6.5 ms) counterparts, and higher SAR pulses outperform their lower SAR counterparts. One observation from the experimental data that may not be immediately obvious in simulations is that, in many cases, higher SAR pulses result in only very subtle improvements. For example, comparison of the low-SAR and high-SAR 6.5 ms OPT-C signal gains in either the central slice or over the entire volume reveals the two pulses to be similarly effective. The whole-volume mean signal gains reported in Table 1 reflect this trend and even reveal slight improvements for low-SAR pulses over high-SAR pulses, as in the case of the 12.9 ms BIR-4. While this phenomenon is likely due to the fact that the optimization region extends over a much larger region in the $B_1^+ - \Delta B_0$ space than is relevant to the field variations observed in the phantom, it does emphasize that increases in SAR are not always necessary to achieve improvements in non-selective refocusing at 7 T. Finally, it is noteworthy that performance of the VS pulse is quite impressive despite the fact it was designed almost 20 years ago and not for the specific purpose at hand. While the cost function value associated with the VS pulse is adversely affected by the lowest $B_1^+$ regions of the optimization grid, these values are not observed in the phantom, and the resulting mean signal gain exceeds that of any other pulse.

Results for the human brain corresponding to Figures 4 and 5 are given in Figures 6 and 7, respectively. In many ways, pulse performance observed in the brain correlates closely with that observed in the phantom; however, high-SAR pulses appear to have a more distinct advantage in the *in vivo* case. This is probably because the field distributions observed in the brain more closely match the values targeted in pulse optimizations, and, as cost function values improve with increased SAR, so do actual *in vivo* signal gains. The VS pulse loses some ground to other high-SAR pulses when compared in this context due to the fact that lower $B_1^+$ values are observed in the brain than in the phantom. It is unclear whether further power calibration of the VS pulse could resolve this issue, although this would certainly require an increase in SAR. Another notable difference between phantom and *in vivo* results is highlighted in the right frontal cortex, a region in which off-resonance performance can be evaluated experimentally (see Figure 2). Signal gains in this area are in general decidedly lower (and even < 1 in some cases, thus implying signal loss relative to the BLK pulse). Thus, a major weakness in many of the evaluated pulse designs appears to be off-resonance performance, thus increasing the appeal of the COMP3 pulse for practical use. We believe this in a relatively minor issue, however, that can be remedied through slight adjustments to the $B_0$ shimming protocol and/or the designated optimization region on the $B_1^+ - \Delta B_0$ grid. Whole-volume signal gains as reported in Table 1 are considerably lower for the brain than for the phantom—an observations that has a two-fold explanation. Foremost is the central region of the phantom in which high $B_1^+$ values (never realized in the brain, Figure 2) result in almost complete signal loss for the BLK pulse, thus relative signal gains for other pulses are exceptionally large (even greater than a factor of 10) in this area. Secondly, the

diminished off-resonance signals of the optimized pulses contribute to lower mean signal gains. Nevertheless, considerable overall signal gains of 7, 17, and 20% are observed in the brain for the 12.9 ms low-, moderate-, and high-SAR OPT-C, respectively, and larger improvements are likely possible with more customized pulse optimizations.

## 5. Conclusion

Using a 3-D SE-EPI sequence, we have investigated the performance of an array of non-selective refocusing pulses in the context of 7 T human brain imaging. Furthermore, we have demonstrated that constrained numerical optimizations can be used to successfully tune adiabatic and composite refocusing pulses given for practical use in this context. To facilitate comparison, pulses were divided into three SAR classes (low, moderate, and high) and two duration classes (≤ 6.5 ms and 12.9 ms). Identification of the pulses in each family with the best performance depends not only on the given application but also on the compromises deemed acceptable by researchers and clinicians.

In light of such performance characteristics that are not necessarily quantifiable in terms of a cost function, we have attempted to outline the major pros and cons of the various pulses included in this study so as to facilitate this decision making process. As stated above, however, differences in many cases are subtle and, depending on the desired level of performance, one could be just as well off to choose the pulse for which implementation is most straightforward as long as customized tuning of the pulse is performed. The results of this work certainly suggest that this is a reasonable criterion. Nevertheless, we have used the various performance metrics of this study to recommend the following pulses within each classification: the 12.9 ms OPT-C pulses are recommended as the best all-round performers in each of the three SAR classes; the COMP3 pulse is a recommended alternative when high bandwidth or very short duration is required; assuming SAR is a primary concern for SE imaging at 7 ms, the low-SAR OPT-C pulses are recommended with the duration dictated by the targeted tissue contrast.

As for future studies, further customization of optimizations through targeting only the $B_1^+$ and $\Delta B_0$ that are observed in the brain at 7 T appears to be a priority. This could be accomplished by obtaining field maps for a large sample of volunteers with differing head sizes. From this data, a suitable set of $B_1^+ - \Delta B_0$ pairs could be determined to guide future optimizations. This process would likely result in improved $B_1^+$ and off-resonance performance while allowing for comparable or even reduced SAR levels. The fact that the pulses considered in this study are exclusively non-selective, limiting use to 3-D sequences in most cases begs that a similar comparison be performed for slice-selective refocusing pulses. The composite pulses in this study may prove translatable to slice-selective forms by changing component pulse shapes from blocks to sincs or Gaussians while incorporating an oscillating slice-selection gradient (e.g., [28, 30, 31, 32]). Although the HS pulses tested in the non-selective context of this study do not stand out as the top performers, these pulses have been shown to exhibit adaptability in the face of SAR-limited optimizations. Therefore, similarly tuned HS pulses may prove to be an excellent choice for slice-selective refocusing even if implemented in a composite form (e.g., [4, 5]) or in conjuction with a quadratic phase excitation (e.g., [6]).

## Acknowledgments

The authors would like to acknowledge helpful conversations with Dr. Richard Dortch and Dr. Mark Does at the Vanderbilt University Institute of Imaging Science and with Dr. Stefan Fischer at Philips Healthcare. This work was supported by NIH (BRP) grant number RO1EB000461.

## References


1. Feinberg DA, Oshio K. GRASE (gradient- and spin-echo) MR imaging : a new fast clinical imaging technique. Magn Reson Med. 1991; 181:597–602.
2. Uğurbil K, Garwood M, Rath AR, Bendall MR. Amplitude- and frequency/phase-modulated refocusing pulses that induce plane rotations even in the presence of inhomogeneous $B_1$ fields. J Magn Reson. 1988; 78:472–497.
3. Staewen R, Johnson A, Ross B, Parrish T, Merkle H, Garwood M. 3-D FLASH imaging using a single surface coil and a new adiabatic pulse, BIR-4. Invest Radiol. 1990; 25:559–567. [PubMed: 2345088]
4. Conolly S, Nishimura D, Macovski A. A selective adiabatic spin-echo pulse. J Magn Reson. 1989; 83:324–334.
5. Hwang TL, van Zijl PCM, Garwood M. Broadband adiabatic refocusing without phase distortion. J Magn Reson. 1997; 124:250–254. [PubMed: 9169217]
6. Park JY, Garwood M. Spin-echo MRI using $\pi/2$ and $\pi$ hyperbolic secant pulses. Magn Reson Med. 2009; 61:175–187. [PubMed: 19097200]
7. Levitt M, Freeman R. Compensation for pulse imperfections in NMR spin-echo experiments. J Magn Reson. 1981; 43:65.
8. Poon CS, Henkelman RM. 180° refocusing pulses which are insensitive to static and radiofrequency field inhomogeneity. J Magn Reson. 1992; 99:45–55.
9. Poon CS, Henkelman RM. Robust refocusing pulses of limited power. J Magn Reson. 1995; 116:161–180.
10. Conolly S, Glover G, Nishimura D, Macovski A. A reduced power selective adiabatic spin-echo pulse sequence. Magn Reson Med. 1991; 18:28–38. [PubMed: 2062239]
11. Ordidge RJ, Wylezinska M, Hugg JW, Butterworth E, Franconi F. Frequency offset corrected inversion (FOCI) pulses for use in localized spectroscopy. Magn Reson Med. 1996; 36:562–566. [PubMed: 8892208]
12. Tannús A, Garwood M. Improved performance of frequency-swept pulses using offset-independent adiabaticity. J Magn Reson A. 1996; 120:133–137.
13. Tannús A, Garwood M. Adiabatic pulses. NMR in Biomedicine. 1997; 10:423–434. [PubMed: 9542739]
14. Sacolick LI, Rothman DL, de Graaf RA. Adiabatic refocusing pulses for volume selection in magnetic resonance spectroscopic imaging. Magn Reson Med. 2007; 57:548–553. [PubMed: 17326179]
15. Balchandani P, Pauly J, Spielman D. Slice-selective tunable-flip adiabatic low peak-power excitation pulse. Magn Reson Med. 2008; 59:1072–1078. [PubMed: 18429017]
16. Schulte RF, Le Roux P, Vogel MW, Koenig H. Design of phase-modulated broadband refocusing pulses. J Magn Reson. 2008; 190:271–279. [PubMed: 18320623]
17. Henning A, Fuchs A, Murdoch JB, Boesiger P. Slice-selective FID acquisition, localized by outer volume suppression (FIDLOVS) for $^{1}$H-MRSI of the human brain at 7 T with minimal signal loss. NMR in Biomedicine. 2009; 83:683–696. [PubMed: 19259944]
18. van Kalleveen IM, Boer VO, Luijten P, Zwanenburg JJ, Klomp DW. Adiabatic turbo spin echo for human applications at 7T. Proceedings of the International Society of Magn Reson Med. 2011; 19:600.
19. Silver M, Joseph R, Hoult D. Highly selective $\pi/2$ and $\pi$ pulse generation. J Magn Reson. 1984; 59:347–351.
20. Silver M, Joseph R, Hoult D. Selective spin inversion in nuclear magnetic resonance and coherent optics through an exact solution of the bloch-riccati equation. Phys Rev A. 1985; 31:2753–2755. [PubMed: 9895827]
21. Moore J, Jankiewicz M, Zeng H, Anderson AW, Gore JC. Composite RF pulses for B1+-insensitive volume excitation at 7 Tesla. J Magn Reson. 2010; 205:50–62. [PubMed: 20451430]
22. Moore J, Jankiewicz M, Anderson A, Gore J. An optimized composite refocusing pulse for ultra-high field MRI. Proceedings of the International Society of Magn Reson Med. 2010; 18:2859.

23. Moore J, Jankiewicz M, Anderson A, Gore J. Hyperbolic secant parameter optimization for non-selective inversion at 7 T. Proceedings of the International Society of Magn Reson Med. 2010; 18:2858.
24. Levitt M, Ernst R. Composite pulses constructed by a recursive expansion procedure. J Magn Reson. 1983; 55:247–254.
25. Center for Devices and Radiologic Health. Guidance for the submission of premarket notifications for magnetic resonance diagnostic devices. Food and Drug Administration; 2003.
26. Bendall MR, Pegg DT. Theoretical description of depth pulse sequences, on and off resonance, including improvements and extensions thereof. Magn Reson Med. 1985; 2:91–113. [PubMed: 3831687]
27. Hornak J, Szumowski J, Bryant R. Magnetic field mapping. Magn Reson Med. 1988; 6:158–163. [PubMed: 3367773]
28. Zelinski AC, Wald LL, Setsompop K, Alagappan V, Gagoski BA, Goyal VK, Adalsteinsson E. Fast slice-selective radio-frequency excitation pulses for mitigating B^1+ inhomogeneity in the human brain at 7 Tesla. Magn Reson Med. 2008; 59:1355–1364. [PubMed: 18506800]
29. Jezzard P, Balaban RS. Correction for geometric distortion in echo planar images from $b_0$ field variations. Magn Reson Med. 1995; 34:65–73. [PubMed: 7674900]
30. Matson GB, Kaiser LG, Young K. New slice-selective pulse cascades produsing uniform tipping in inhomogeneous rf fields. Proceedings of the International Society of Magn Reson Med. 2007; 15:1682.
31. Boulant N, Cloos MA, Amadon A. $B_1$ and $B_0$ inhomogeneity mitigation in the human brain at 7 T with selective pulses by using hamiltonian theory. Magn Reson Med. 2011; 65:680–691. [PubMed: 20949589]
32. Moore J, Jankiewicz M, Anderson A, Gore J. B1+-insensitive slice-selective pulses constructed from optimized non-selective composite waveforms. Proceedings of the International Society of Magn Reson Med. 2011; 19:2912.

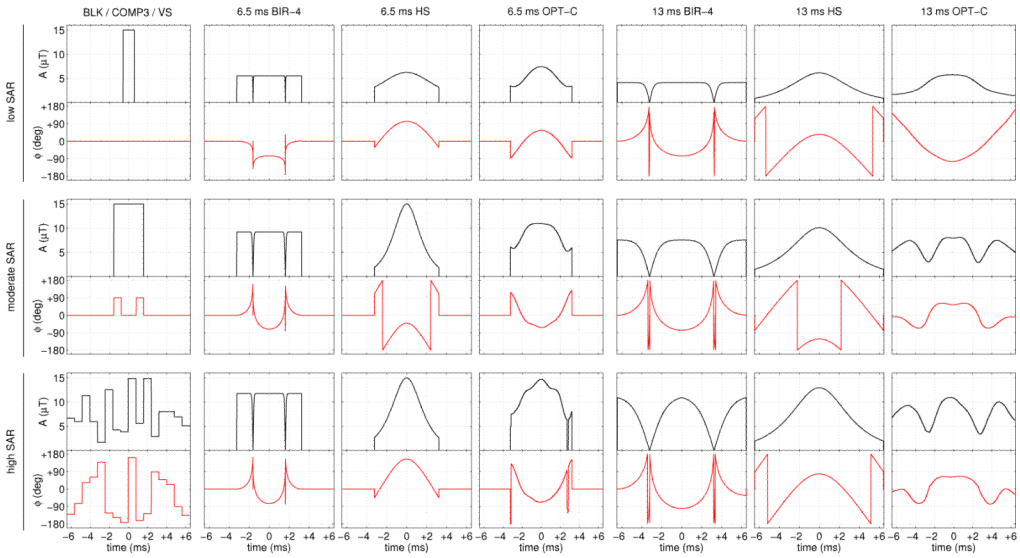


**Figure 1.**

Amplitude (black) and phase (red) modulation waveforms for all 21 refocusing pulses evaluated in this study. Plots are organized such that rows correspond to refocusing SAR categories and columns correspond to pulse type. In the first column, the BLK, COMP3, and VS pulses appear in descending order. In any other given column, waveforms correspond to a single pulse type (i.e., BIR-4, HS, or OPT-C) with the indicated total duration.

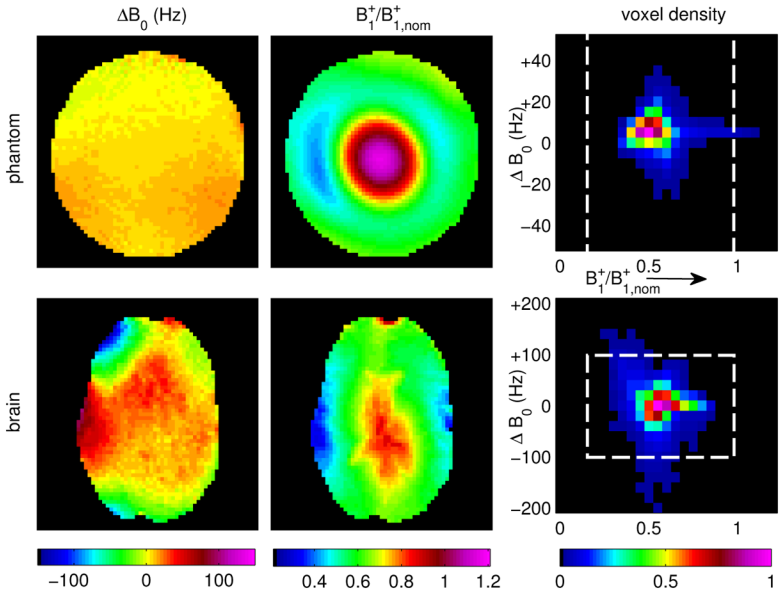


**Figure 2.**

Maps of $\Delta B_0$ (left column) and $B_1^+/B_{1,\mathrm{nom}}^+$ (middle column) as measured in the central axial slice of the phantom (top row) and the human brain (bottom row). In the right column are 2-D histograms of relative voxel density over grids of $B_1^+$ and $\Delta B_0$ values as measured for all voxels in each 3-D volume (i.e., not only for the slices appearing in columns 1 and 2). Dashed white lines indicate the boundaries of the region targeted in RF pulse optimizations.

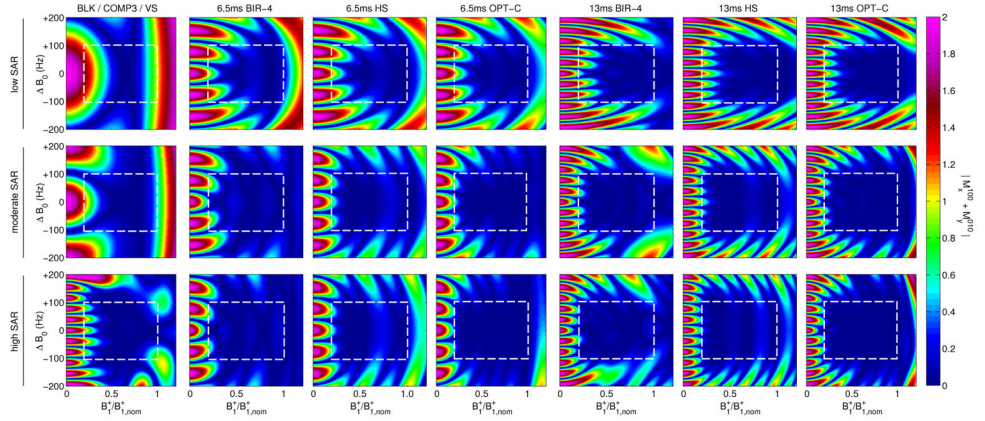


**Figure 3.**

Simulation results indicating performance of refocusing pulses on $B_1^+ - \Delta B_0$ grids relevant to 7 T brain imaging. Plots are organized in the same manner as Figure 1, with rows corresponding to refocusing SAR categories and columns corresponding to pulse type. The color scale reflects the value of $M_x^{100}+M_y^{010}$ (see Equation 3) where the three superscripted numbers give the initial conditions of $M_x$, $M_y$, and $M_z$, respectively. White dotted lines within each plot indicate the region targeted by optimizations. Within this region of interest, performance among pulses varies subtly but tends to improve with increasing SAR and increasing duration.

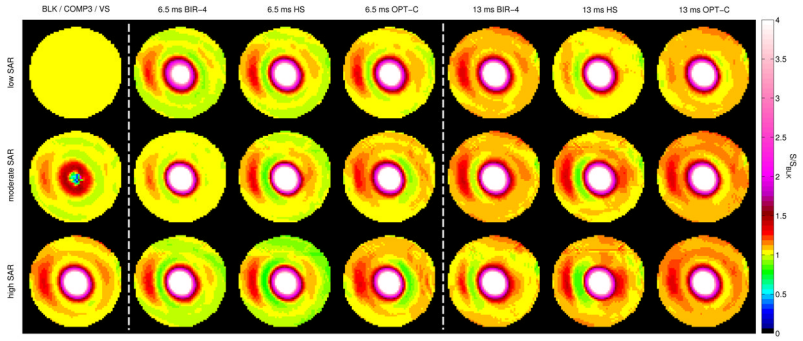


**Figure 4.**

Ratios of SE-EPI signal to that obtained with the BLK refocusing pulse for the central axial slice of the phantom at 7 T. Results are organized in the same manner as Figure 1, with rows corresponding to refocusing SAR categories and columns corresponding to pulse type. Although the ~ 13 ms OPT-C pulse may exhibit the best performance in the given slice, the ~ 13 ms BIR-4 pulse appears to result in similar signal gain at a much reduced SAR. Within the group of 6.5 ms pulses (columns 2–4), the OPT-C pulse appears an attractive low-SAR option while the high-SAR counterpart offers only modest signal gains in comparison.

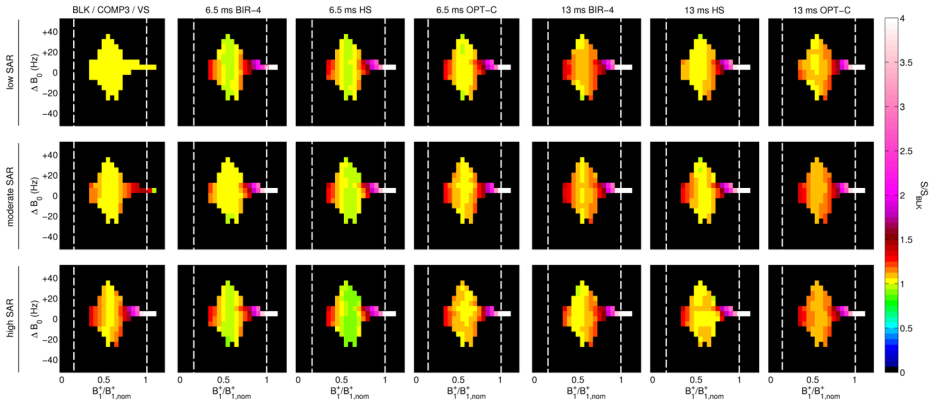


**Figure 5.**

Average signal gains for the entire phantom volume shown as a function of $B_1^+$ ($x$ axis) and $\Delta B_0$ ($y$ axis). Each data point represents $S/S_{BLK}$ values averaged for all voxels falling within a discrete interval of $B_1^+$ and $\Delta B_0$. With the exception of the COMP3 pulse, all pulses result in very high signal gains in the central (high- $B_1^+$) regions of the phantom. From these results alone, it appears the ~ 13 ms BIR-4 pulse is the best low-SAR choice and the ~13 ms OPT-C pulses the best choices for moderate- and high-SAR applications.

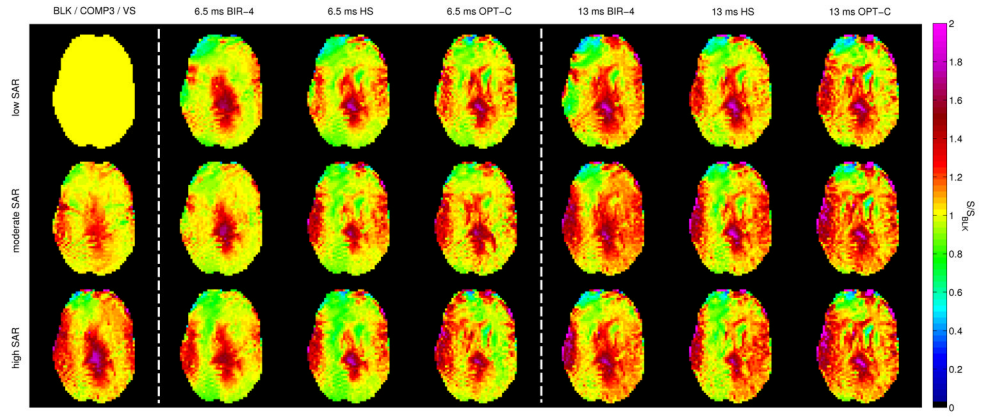


**Figure 6.**

Ratios of SE-EPI signal to that obtained with the BLK refocusing pulse for the central axial slice of the *in vivo* human brain at 7 T. Results are organized in the same manner as in Figure 1, with rows corresponding to refocusing SAR categories and columns corresponding to pulse type. Generally, refocusing performance is well matched to the phantom observation reported in Figure 4; however, $B_0$ offsets in the right frontal lobe (see Figure 2) allow for a more rigorous test of bandwidth limitations. In accordance with simulations, shorter pulses (columns 2–4 and COMP3) appear more robust in the face of these large $B_0$ variations.

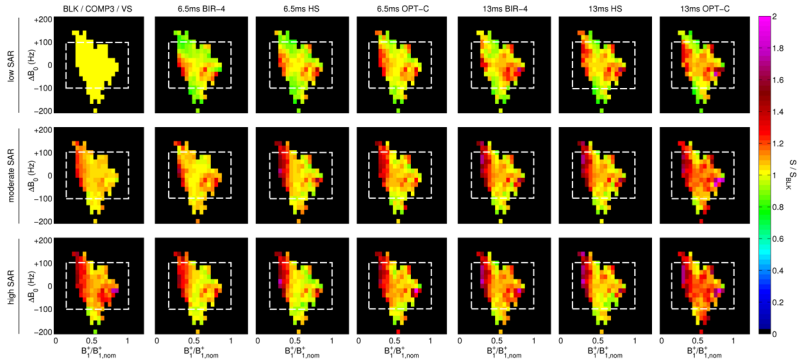


**Figure 7.**

Average signal gains for the entire brain volume shown as a function of $B_1^+$ ($x$ axis) and $\Delta B_0$ ($y$ axis). Each data point represents $S/S_{\mathrm{BLK}}$ values averaged for all voxels falling within a discrete interval of $B_1^+$ and $\Delta B_0$.

**Table 1**

Selected attributes and performance metrics for all pulses in this study. Included are: the total pulse duration ($\Delta T$); the minimum repetition time ($T_{R,\min}$) that allows for adherence to a SAR limit of 3 W/kg; a measure of SAR as calculated from $\int |A(t)|^2\, dt$; the theoretical refocusing performance as measured by evaluating the cost function ($\delta$, Equation 3) within the targeted optimization region; the mean experimental signal ratios ($S/S_{\mathrm{BLK}}$) with respect to signal obtained using the BLK pulse for the entire volume of both the phantom and the human brain. Grouping by rows reflects the *low*, *moderate*, and *high* SAR classes described in the text.

| SAR class | pulse name | $\Delta T$ [ms] | $T_{R,\min}$ [ms] | $\int \lvert A(t)\rvert^2 dt$ [$\mu$T$^2$ · ms] | $\delta$ | $\frac{S}{S_{\mathrm{BLK}}}$ phantom | $\frac{S}{S_{\mathrm{BLK}}}$ brain |
|---|---|---|---|---|---|---|---|
| low | BLK | 1.2 | 162 | 265 | 0.994 | 1.00 | 1.00 |
| | BIR-4 | 6.5 | 119 | 196 | 0.806 | 1.11 | 1.00 |
| | | 12.9 | 119 | 196 | 0.716 | 1.33 | 1.06 |
| | HS | 6.5 | 103 | 168 | 0.779 | 1.19 | 1.01 |
| | | 12.9 | 114 | 187 | 0.615 | 1.25 | 1.05 |
| | OPT-C | 6.5 | 120 | 196 | 0.694 | 1.21 | 1.03 |
| | | 12.9 | 120 | 196 | 0.566 | 1.27 | 1.07 |
| moderate | COMP3 | 2.4 | 324 | 530 | 0.510 | 1.06 | 1.07 |
| | BIR-4 | 6.5 | 320 | 524 | 0.445 | 1.24 | 1.06 |
| | | 12.9 | 320 | 524 | 0.300 | 1.32 | 1.10 |
| | HS | 6.5 | 320 | 524 | 0.345 | 1.22 | 1.08 |
| | | 12.9 | 307 | 503 | 0.263 | 1.28 | 1.10 |
| | OPT-C | 6.5 | 320 | 524 | 0.269 | 1.26 | 1.09 |
| | | 12.9 | 320 | 524 | 0.232 | 1.27 | 1.17 |
| | VS | 12.9 | 551 | 904 | 0.514 | 1.30 | 1.13 |
| high | BIR-4 | 6.5 | 520 | 852 | 0.276 | 1.22 | 1.07 |
| | | 12.9 | 519 | 852 | 0.195 | 1.27 | 1.13 |
| | HS | 6.5 | 361 | 592 | 0.319 | 1.18 | 1.06 |
| | | 12.9 | 506 | 829 | 0.182 | 1.27 | 1.09 |
| | OPT-C | 6.5 | 520 | 852 | 0.136 | 1.25 | 1.11 |
| | | 12.9 | 520 | 852 | 0.108 | 1.25 | 1.20 |